Oceanic Kelvin Waves and Tropical Atlantic intraseasonal Variability.

Part I: Kelvin wave characterization.

Irene Polo (1), Alban Lazar (2), Belen Rodriguez-Fonseca (1), Sabine Arnault (2)

(1) Departamento de Geofísica y Meteorología, Facultad de C.C. Físicas. UCM, Av/ Complutense 28040-Madrid, Spain.

(2) LOCEAN - IPSL / Univ. Paris VI. 4 pl. jussieu, 75252 Paris cedex 05, France

Corresponding author address: Irene Polo. Departamento de Geofísica y Meteorología, Facultad de C.C. Físicas. UCM, Av/ Complutense 28040-Madrid, Spain.

Phone: 0034-91-394-4440

Email: ipolo@fis.ucm.es

Abstract

Oceanic Kelvin waves from the equator to the West African coast are investigated in the framework of Tropical Atlantic (TA) intraseasonal variability. In order to better highlight the wave propagations, a 25-95 day band-pass filter was applied to the Sea Surface Height (SSH) product derived from the TOPEX/Poseidon altimeter and an OGCM simulation for the 1993-2000 period. In addition to equatorial eastward propagations, our analysis reveals recurrent and continuous propagations distinguishable over thousands of kilometers poleward along the coasts as far as about 10-15 degrees of latitude, a novel result with altimeter data. The variance of the filtered SSH signal goes from 1 cm at the equator to 2 cm at the African coast. Estimates of the phase speed range from 1.5 m/s to 2.1 m/s along the equator and the West African coastline. Such values are very close to those of equatorial Kelvin wave propagations, likely dominated by the first two baroclinic modes, supporting the fact that the coastal propagations are coastally trapped Kelvin waves. In order to simplify the description of these Kelvin waves, we present an intraseasonal climatology which reveals regular boreal autumn-winter equator to coast propagations. An improved description is achieved thanks to the computation of an extended empirical orthogonal function for the boreal autumn-winter propagations. Lag correlation of SSH signals allows for a twofold quantification; the phase speed and the importance of remote forcing along the coast. The remote forcing effect of intraseasonal Kelvin waves is clearly evidenced over coastal upwelling regions as far as 10-15 degrees latitude. The physical mechanism associated with the forcing of the Kelvin waves and its impacts are investigated in Part II of this work.

1 Introduction

Most of the heat content variability in the tropical ocean is located in the upper layer and, as a result, low latitude oceans are often approximated as a two-layer system. This attribute approximation implies that variations in the depth of the thermocline, and hence of the heat content, are directly reflected in Sea Surface Height (hereafter SSH, Rebert et al., 1985) with the first baroclinic mode being dominant.

As shown by Matsuno (1966) and Moore (1968), the latitude band of the tropical oceans is the site of a singular set of equatorial waves that propagate eastward (equatorial Kelvin waves) or westward (Rossby waves). Their sea-level signature is adequate to their detection and satellite altimeters can measure the signals down to a few centimetres. Although altimeter measurements primarily reflect the movement of the thermocline, because of the near-surface intensification of baroclinic modes (Stammer, 1997), second and third baroclinic modes could also be important in the actual Tropical Atlantic (du Penhoat and Trequier, 1985; Illig et al., 2004; Shouten et al, 2005). The phase speed estimated of the equatorial Atlantic is 2.6 m/s for the first vertical mode Kelvin wave, and 1.4 m/s and 0.8 m/s for the second and third vertical modes (Schouten et al., 2005; Illig et al., 2004).

The Tropical Atlantic (TA) dynamic sea level variability is dominated by the seasonal cycle (Arnault and Cheney, 1994). The seasonal adjustment of the ocean to the forcing of the wind stress causes a cycle of consecutive Rossby and Kelvin waves. Figure 1a shows the seasonal cycle of the sea level and the wind stress along the equator and the West African coast. This standard figure (similar to the one shown by Shouten et al., 2005 and Rouault et al., 2007) computed here as the sum of the annual and semiannual harmonics, is characterized at the eastern equator by an upwelling season (May to October) and a downwelling season (November to April), coinciding with the strengthening and weakening of the trade winds at the equator. Along the coast of the Gulf of Guinea (GG), coinciding with the two upwelling seasons (February-March and August-September; Picaut, 1983), there are some apparent coastal propagations of the sea level (February-March and August-September in figure 1a-left) which, are slower than the one expected from theoretical first mode Kelvin wave propagations (Schouten et al., 2005) and whose wave nature is not clear. One might wonder from this figure whether there are only high-order slow modes along the coast, or if the lowest-order baroclinic modes are masked by wind changes associated with the ITCZ migration or other large-scale processes. In order to answer this question an additional processing of the signal is thus necessary to verify the latter-mentioned coastal propagations.

Since Matsuno (1966) established the equations of the shallow water equatorial waves, several studies early advocated the idea that part of the equatorial and coastal upwelling in the GG is remotely forced by the wind in the western equatorial Atlantic via Kelvin waves (Moore et al., 1978; Adamec and O'Brien, 1978; O'Brien et al., 1978; Clarke, 1978; Servain et al., 1982). Further elements were presented in support of coastal wave propagation in the TA with Sea Surface Temperature (SST, Picaut, 1983) and tide gauges records (Aman et al., 2007). A new stage started when TOPEX/Poseidon (T/P) was launched in 1992 and, since then, Kelvin wave propagations have been better described in the equatorial Atlantic (Katz, 1997; França et al., 2003; Illig et al., 2004; Schouten et al., 2005; Han et al., 2008) and equatorial Pacific (Kessler et al., 1995; Meyers et al., 1998; Cravatte et al., 2003; Roundy and Kiladis, 2006). These studies used band-pass filters in order to avoid the masking effect of large-scales signals and this is also the strategy we adopted in this paper.

Regarding theoretical studies about the continuity of the equatorial Kelvin waves along the eastern boundary, Moore (1968) established that the equatorial Kelvin waves could be reflected in the eastern boundary, and in part, could propagate poleward coastally trapped. Although Clarke (1983) also established analytically the equatorial wave reflection in an oceanic boundary, he found that the reflection occurred without dissipation. Greatbatch and Peterson (1996) described how the stratification changes could slow down the coastally trapped wave propagation in high latitudes. Using observational data, convincing elements have been presented of Kelvin wave propagations from the equator to the coast in the eastern Pacific at intraseasonal (Hormazabal et al., 2002), and interannual timescales, especially during ENSO events (Jacobs et al., 1994; Meyers et al., 1998; Vega et al., 2003). Grodsky and Carton (2006) have found coherent interannual variations of SSH in the equatorial Atlantic and the southern subtropical Atlantic. They hypothesized that a link between the two is provided by coastal waves propagating southward along the African coast.

Along the coast, one way of dissipation of the Kelvin wave energy is the radiation of Rossby waves from the eastern boundary (Gill, 1982). The Rossby wave when reaching the western boundary can then potentially trigger a new Kelvin wave at the western equator. However several works have argued that the small Atlantic basin and the presence of the North Brazil Current (NBC) could inhibit the Rossby reflection (Arnault et al., 1990, Handoh and Bigg, 2000, Illig et al., 2004). These authors have experienced difficulties at tracking back equatorial waves up to the American coast.

In this paper, we have focused our analysis on intraseasonal timescales. At these scales, the Kelvin wave activity has been pointed out, mainly in the Pacific basin, to be associated with the convection activity, which can be important in climate terms (Kessler et al., 1995; Hendon et al., 1998; Roundy and Kiladis, 2006). In the TA, intraseasonal variability modulates the main annual to interannual basin signals of important processes (i.e. West African Monsoon, oceanic cold tongue over the eastern equatorial Atlantic, seasonal coastal upwelling at the African West coast, etc…). Therefore it is important to investigate the nature of the intraseasonal SSH signal, and in particular its contribution to the teleconnection processes within the tropics. Furthermore, an unambiguous detection of continuous propagating signals from the equator to the subtropical along the eastern Atlantic ocean coastlines at intraseasonal scales is still missing, and we understand there is a need of filling this gap through further investigation. It is the goal of this first paper to provide a sound description of this phenomenon over the TOPEX/Poseidon 1993-2000 time period, using the satellite measurements combined with an Ocean General Circulation Model (OGCM) simulation. In the second part of this paper, we analyse the various forcing of these waves as well as some of its impacts in relation to the TA intraseasonal variability. The current manuscript presents a detailed description of the data used (section 2). After a discussion of the choice of the band-pass filter (section 4), we study the intraseasonal propagating SSH anomalies in the observations and the OGCM (section 5), through a climatology and, focusing on boreal autumn-winter season, the main propagating mode. Then apparent propagation phase speeds are quantified and the remote impacts characterized (section 6). Finally the main conclusions are summarized.

2 Description of the data

We use SSH TOPEX/Poseidon altimetry measurements, with 0.5 degrees horizontal resolution and 7-days time resolution produced and distributed by Aviso, as part of the Ssalto ground processing segment. The T/P SSH anomalies have already been corrected by removing four-year average elevation and signals such as the ocean tide, the dry tropospheric, inverted barometer, tidal aliasing and vapour water. The inter-comparison analyses with *in situ* measurements (i.e. tide gauges records) have demonstrated that the altimetry is an important tool to observe oceanic variability (Arnault et al., 1992), even in the coastal regions (Aman et al., 2007). In contrast to the sparse network of coastal tide gauges, measurements of SSH from space by satellite radar altimetry provide near global and homogeneous coverage of the world's oceans. The weekly temporal resolution of the T/P SSH is expected to be high enough for the description of the baroclinic Kelvin waves, since the theoretical first baroclinic mode takes about 30-45 days to cross the Atlantic along the equator and more than 20 days to leave the tropical latitudes studied here. However, the 0.5 degree spatial resolution corresponds to the Rossby radius of deformation at about 15 degrees of latitude for a 2 m/s baroclinic phase speed. Therefore it is certainly a limitation to our analysis, and it may in particular affect our ability to observe coastal waves poleward of 10 to 20 degrees of latitude.

In order to complete the study with synchronous subsurface oceanic quantities that are not available in the observations, in particular the thermocline depth, we use a numerical simulation of the OPA OGCM (Madec et al., 1998). The ORCA05 configuration used here was run at the LOCEAN laboratory by the NEMO (Numerical Framework for Ocean Modeling) team, for the 1992-2000 period. The configuration is for the global ocean with a 0.5 degrees horizontal resolution and 30 vertical levels. The momentum flux is the weekly ERS1-2 wind stress interpolated daily, while the air-sea heat fluxes are computed in line with semi-empirical, or bulk formulas using OGCM SST, the ERS1-2 wind speed, the NCEP-NCAR reanalysis (Kalnay et al., 1996) air temperature, and monthly climatological air humidity (Trenberth et al., 1989) and cloudiness (Berliand and Strokina, 1980). Precipitation data come from the Climate Prediction Center Merged Analysis of Precipitation (CMAP) product (Xie and Arkin, 1996). Major river runoffs are taken into account through monthly values of river discharge (UNESCO, 1996). At last, a restoring term towards Levitus (1998) Sea Surface Salinity is applied to the fresh water budget. For further details on the model configuration see de Boyer-Montégut et al. (2007).

In this work we have used 5-day average output of SSH and 18°C isotherm depth (hereafter z18). We have chosen the 18°C isotherm depth as the thermocline depth proxy after having analysed the isotherms ranging from 15°C to 25°C. The 18°C isotherm depth appears to be the most representative thermocline proxy over the African coastlines, in particular within upwelling areas where the isotherms outcrop. Note that the pycnocline (represented as sigma-26 isopycnal depth $z\sigma 26$) is theoretically more closely related to waves and it has more physical meaning than z18. However the z18 it is much better geographically defined than $z\sigma 26$, especially in the coastal areas, therefore z18 will be used along the study. In the next section, some basic statistics are performed to show the ability of the model to reproduce the SSH observations for the 1993-2000 period.

To follow the Kelvin wave propagation, wave-tracks have been defined along the equator and the African coast following the model grid, thus the distance between two grid points is 0.5° (~55 km). For the sake of minimizing data gaps, the northern coastal track-points have been shifted 0.5° offshore. The corresponding wave-tracks are shown in figure 1b, along the equator and poleward along the African coast. For the north, the track moves along the GG westward and continues northward up to 30°N, having twice more track-points than the south. For the south, the track runs up to 25°S along the coast (named hereafter southern African coast). Note that both, north and south wave-tracks, share the first ~120 points corresponding to the equatorial Atlantic. It bears mentioning that following the coastline along different isobaths (0, 200, 400, 1000 meters) does not make substantial differences and no remarkable properties changes are found (not shown). In this paper generally, for the sake of simplicity, the term "Kelvin wave" refers to the equatorial and coastally trapped propagations, even though the coastal wave nature may be a mixed of Kelvin and topographic wave.

3 Interannual SSH anomalies

The annual and semiannual components dominate the sea level variability over the equator and the African coast (Wilson and Adamec, 2002; Schouten et al., 2005; Aman et al., 2007). Figure 2 shows Hovmuller diagrams of the observed SSH interannual anomalies along the wave-tracks, which are the result of removing the seasonal cycle relative to the above-mentioned harmonics to the total signal. The result of this truncation (figure 1a) is similar to the one obtained when performing the seasonal cycle with higher truncation or with a simple climatologycal average (not shown). Although propagations are difficult to identify unequivocally due to basin-scale interannual SSH anomalies (Handoh and Bigg, 2000; França et al., 2003), many propagating-like signals appear strikingly going from the equator to the African coast; along the GG (figure 2-left) and along the southern African coast (figure 2-right). It is also noticeable that some points are particularly noisy: in the western equator (0-20 equatorial track-points), at 5°S (140 south track-point), and at 10°N (200 north track-point). The first two locations correspond to the Amazon and the Congo River run off. Whereas the last location corresponds to the large offshore extension of the continental plateau, likely associated with strong tidal signals.

The diagrams show extreme positive and negative events, associated with the 1995-1996, 1998, 1999 warm events and the 1994, 1997 and 2000 cold events. Some of those years have been described by other authors in relation to a self-sustaining Atlantic climate mode (Handoh and Bigg, 2000), to interannual variability modes (Sutton et al., 2000; Illig et al, 2006), to ENSO (Saravanan and Chang, 2000) and to the extratropical north Atlantic climate variability (Rodriguez-Fonseca et al., 2006). Interestingly, this figure suggests a quasi-permanent intraseasonal modulation of the interannual signals. The aim of the rest of this article is to characterize the intraseasonal SSH component.

4 Selection of the intraseasonal frequency band

Figure 3a presents the energy spectra of the observed SSH along the wave-tracks computed up to a period of 500 days. The annual and semiannual cycles appear the most energetic and are present along the equator and the coast; they are followed by a 120 days signal (top panel). For periods smaller than 100 days, energy is less concentrated in a specific periodicity (bottom panel). However, there are some relative maximum at the 100 to 95 day and 60 to 50 day periods. Below 30 days approximately, there is no energy as expected when reaching close to the T/P time resolution. Periodicity peaks at intraseasonal scales in the Atlantic have been studied in details by Katz (1997) who found enhanced variance at about 25 and 50 days, as well as Han et al. (2008) have found dominant spectral peaks within the intraseasonal windows at 10-40 and 40-60 days. In the Pacific, Kessler et al. (1995) or Cravatte et al. (2003) have also evidenced a peak at 120 days, but the next smaller period is 75 days, with neither 60 days nor 95 days peaks. It appears in the Atlantic with no clear single peak but rather with a wide range of active periods. As Roundy and Kiladis (2006) proposed for the Pacific equatorial Kelvin waves, this spreading of the wave frequencies may occur in part because phase accelerations and amplitude variations are forcing the waves to become not sinusoidal in time.

Figure 3b shows an example of three points along the northern wave-track (x=36, 105 and 168, which correspond to western equator, eastern equator and GG respectively). Although depending on the location the SSH signals differ (figure 3b-bottom panel), the power spectrums from 100 to 25 days, show a relative peak in between 67-50 days (figure 3b-top panel).

Finally we chose to retain the 25-95 day periodicity. The filter has been performed by subtracting two low-pass filters, which have been constructed by smoothing the signal with a Hanning weighting function of 21 days and 91 days time-window, respectively (25-95 days for the modelled data). The smoothing replaces each value on the grid to which they are applied with a weighted average of the surrounding data values along the time axis. The subtraction of the two low-pass filters results in a 25-95 day band-pass filter, whose frequency response function (not shown) preserves about 60% of the signal amplitude within the 70-35 day band, with a maximum (80%) at 50 days, and a 10% preserving reached at about 200 and 20 day periods. Note that the filter preserves the frequencies, and it neither creates artificial spectral peaks nor phase shifts associated with negative lobes.

5 Description of the intraseasonal Kelvin wave propagations

Figure 4a shows the result of filtering the T/P SSH data in the entire period along the north (left panel) and south (right panel) wave-tracks. It can be noticed the almost-permanent eastward/poleward propagating signals along the year and for all the years. A first gross visual estimation of the slopes for continuous signals suggests a regular propagation phase speed of ~1.8 m/s. The diagram shows downwelling and upwelling Kelvin wave propagation with a ~2 month period. It is important to notice that, although the filter is preserving the 50 day period, the 2 month period signal is not just a filter product since figure 3 support the importance of the 2 month period, and similar SSH signals are found when filtering the SSH within different windows (i.e. 25-150 day band, not shown).

The absolute mean value of the SSH signal amplitude is 1-2 cm at the equator and the signal is amplified to 2-4 cm at the beginning of the coast, at the coast of the GG (from 120 to 180 north track-points) and at the southern African coast (from 120 to 150 south track-points). This intraseasonal SSH signal represents approximately 50% of the seasonal cycle amplitude (comparing with figure 1a). The SSH variance (figure 4b) shows 1 cm at the equator that increases at the African coast to 2 cm, with higher variance at some coastal track-points.

Although there are horizontal SSH bands (i.e. October-November 1993; October-November 1997 in figure 4a), corresponding to a whole basin equatorial events, most of the SSH signals are associated with an eastward propagation. After the equatorial Kelvin wave splits at the African coast, poleward propagation can be noticed as far as 12 degrees (200 north track-point and 160 south track-point). Beyond these points, no propagation can be detected. Some exceptions, as for the southern track, that shows clearer propagation at higher latitudes for some events (see November-December 1993 events in figure 4a), could be due to some “in phase” SSH variations forced locally by wind burst. This latitudinal propagation threshold is explained by the limitation of the data resolution (~0.5°) versus the radius of deformation. Poleward 15 degrees latitude, the distance comprised in 0.5° longitude exceeds the radius of deformation computed for 2 m/s baroclinic phase speed (not shown), which makes the wave to be hardly detectable.

Strikingly, the Hovmuller diagrams repeatedly display equatorial and coastal downwelling Kelvin wave in September, December and March; and whereas equatorial and coastal upwelling Kelvin wave appears frequently in November, January and July.

The September-November and December-January pairs are representative for most years. However, an interannual modulation of the intraseasonal variability is also clear (for example comparing autumn-winter 1994 and 1999 years in figure 4a).

The Hovmuller diagram for the modelled SSH (not shown), exhibits even clearer anomaly propagation at those frequencies than the observed SSH. In order to test the ability of the ORCA05 configuration to simulate the intraseasonal SSH, we have correlated the model and the T/P data at intraseasonal scales (figure 4c). Along the equator the correlation is statistically significant except for the western equatorial Atlantic, because of the noisy SSH signal in this area, as it has been discussed before (likely due to the low time-resolution of the river runoff data in the model, T/P error near the Amazon mouth, or incorrect NBC rings in the model). Along the coast, the correlation is good for most of the points, decreasing poleward for the north and south wave-tracks.

The differences of the variances for the model and for the observations can be seen in figure 4b, being the amplitude of the observations larger than the model one. In particular, the variance differs very much for the point 190 of the north wave-track, a point that is probably very affected by the tide of two month period (Arnault and Le Provost, 1997). The differences at 0-20 equatorial track-points and 140 south track-point are related to the Amazon (not shown because it has a very large value) and the Congo River runoff respectively. The main differences also appear at 220-240 north track-points and 185 south track-point, which correspond to the permanent coastal upwelling regions, likely not very well represented by the altimetry and/or due to the model resolution. Note that the correlation between the modelled and observed non-filtered SSH data is statistically significant for all the points (not shown), although the lower correlation occurs at the GG for the north wave-track and at 15°S for the south wave-track (r=0.5). Although a thorough inter-comparison study between the model and the T/P data is out scope of our work, the statistical basic test suggests that the model configuration is suitable to study the SSH intraseasonal variability at the equator and the tropical African coast. Hereafter, the model and the observations will be used along the paper to understand the SSH variability, as well as its dynamics in the companion paper. At last, it is worth noting that the same Hovmuller diagram as figure 4a for the modelled z18 variable (not shown) displays similar characteristics in term of propagation, suggesting that the observed SSH is a very good proxy for the study of propagations in the real thermocline. This is in agreement with studies of the relationship between sea level and stratification in the tropics, which have suggested that a 1-2 cm rise in the sea level reflects a 2-4 m deepening of the thermocline (Carton et al., 1996).

5.1 Intraseasonal climatology: Main recurring propagation

To clarify the main propagation properties described before, and particularly bring to light the most regular intraseasonal signals, the 5-day climatological average of the band-pass filtered SSH for the period 1993-2000 has been computed for the observations and the simulation. This intraseasonal climatology (figure 5a) displays some events clearly related to wave propagations, along parts of the tracks. The equator shows more positive propagation during the downwelling season (September to February, figure 1a), and more negative and quite less propagating signals during the climatological upwelling season of the western basin (March to August). The most pronounced features in figure 5a appear in the boreal autumn-winter season, in particular September and December downwelling propagations. They are associated with November and January upwelling propagations, they seem to reach quite far poleward in both hemispheres, and are comparable in the model and the observations.

The phase speed of these events range from 1.6 m/s (grey arrow) to 1.8 m/s (white and black arrows), the latter corresponds to the one estimated from the figure 4a. The SSH slope suggests that the phase speed slows slightly down from the equator to the African coast.

Despite weaker amplitude compared to the non-averaged signals (figure 4a), the amplitude of this climatology still represents more than 20% of the seasonal cycle amplitude (from figure 1a). In order to represent the significance of this intraseasonal climatology for all the years considered here in observations and model, we have performed a significance parametric test under; on the one hand, the null hypothesis of “equal means” and on the other hand the null hypothesis of “independent fields”. Each year has been compared to the sampled mean constructed without that particular year under 95% and 99% confidence levels. The mean is statistically significant, at 95% and 99% confidence level, for all the years for observations and model and for north and south wave-tracks (not shown). The correlation is statistically significant at 99% confidence level from a t-test, for most of the years along the track (figure 5b). The observed SSH intraseasonal climatology is significant over the central-eastern equatorial Atlantic for all the years, but it is not significant at the western equatorial Atlantic and subtropical regions (figure 5b right-panel). Regarding the model, the intraseasonal climatology is not significant for some particular years (1997, 1998 and 2000) over central equatorial Atlantic (figure 5b left-panel). The year 1997 does not seem to be significant mostly along both, north and south wave-tracks, and for observations and model. The most significant regions for both, observations and model are the central-eastern equatorial Atlantic, the GG and the southern coast from the equator up to 12°S.

In order to assess the thermocline vertical displacements associated with the SSH anomalies, the intraseasonal climatology of the 18°C isotherm depth is presented in figure 5c (the intraseasonal climatology of the modelled SSH is also superimposed). Whereas the consistency between the SSH and the z18 is high, the latter is often more continuous from the equator to the coast, and further north and south than the former (see the December downwelling wave that reaches the most northern point at approximately constant speed). Note that the SSH and z18 are more in agreement over the equatorial band than poleward of 10° latitude where the SSH-z18 relation is more complex, likely due to larger compensation effects by additional thermodynamical processes such as surface heat fluxes (Mayer et al., 2001).

From z18 intraseasonal climatology (figure 5c), the August-September downwelling Kelvin event can be seen as a particular wave starting at the African coast, rather than propagation from the western equator. At this event there is a different behaviour of the SSH and z18; the z18 splits between the equator and the GG and it is interpreted as split of modes, which is coherent with Illig et al's results (2004). Once trapped at the coast, SSH and z18 September and December donwelling signals appear to be amplified in the coast of the GG (140-200 north track-points) and in the southern coast (120-160 south track-points). This amplification was also noticeable over the whole 93-00 period for the T/P SSH and its variance (figure 4a left panel, and figure 4b). The propagation pattern disappears further 215 north and 170 south track-points, and beyond these points (near subtropics) the signal seems to be stationary (figure 4a, figure 5a and figure 5c).

To isolate and quantify the spatial-temporal structure of the robust September to February Kelvin waves, we present in the next section an Extended Principal Component Analysis.

5.2 A mode for boreal autumn-winter intraseasonal Kelvin waves

A canonical mode of the boreal autumn-winter Kelvin waves can be established thanks to a discriminant analysis technique known as Extended Empirical Orthogonal Functions (EEOF), which constitutes an extension of the traditional EOF technique. It deals not only with spatial but also with temporal correlations observed in weather/climate data (Weare and Nasstrom, 1982), and it is suitable to study oscillatory phenomenon (Fraedrich et al., 1997). We consider positive and negative lagged timeseries for each track-point, and we apply an EOF analysis of this pool of time series. The EEOF analysis recognizes that the temporal evolution of the spatial patterns is an integral part of a system's development. Consider a track–time section (Hovmuller), which can be described by a vector of K components ordered according to the track and evolving with time. Sliding a time window of length W over this vector time series leads to a new vector, this vector represents the states of the system in a $K \times W$ dimensional phase space spanned by time-delay coordinates.

As it has been seen previously, the autumn-winter is a particularly active season for the Kelvin waves, therefore the EEOF analysis is performed for the boreal autumn-winter season (from September to February) for all the years from 1993 to 2000. The EEOF analyses are performed on time wave-track series of observed filtered SSH, and applying a window of 5 days to the data obtaining 21 lags, and thus calculating the EOFs of the time development of the Kelvin wave-track structure. From the analysis, a resultant total Extended Principal Component (EPC) index is computed, which is projected onto the original field to represent the EEOF spatial pattern. For simplicity only the north wave-track is analyzed, since both, north and south wave-tracks share the equatorial Atlantic and the leading mode of the south wave-track (not shown) is highly correlated with the leading mode of the north wave-track.

The leading EEOF variability mode of boreal autumn-winter filtered T/P SSH, which explains 10% of the variance of the filtered signal, is shown in figure 6. It shows the upwelling-downwelling Kelvin waves along the equator and the coast of the GG (figure 6-top panel). The SSH anomalies propagate from the western equator to 15°N approximately (220 track-point) at a rather stable speed ranging from 2 m/s to 2.5 m/s, a higher phase speed than the one estimated from the previous Hovmuller plots. Further north, in the subtropical coastal region other processes seem to explain the SSH variability, as previously discussed. The leading EPC (figure 6-bottom panel) shows one cycle per autumn-winter of positive and negative SSH over the wave-track. The remarkable interannual modulation of the EPC index is in agreement with those noticed previously in figure 4a. Although special years of variability are found for the 1996-1998 period, the main periodicity of the wave from the EEOF analysis is around 50 days. The second mode (not shown) corresponds to Kelvin wave propagation along the western-central equatorial Atlantic (in quadrature-like with the leading mode) but without continuity along the coastal wave-track.

In order to visualize the spatial structure of the leading EEOF mode, the observed SSH over the whole TA basin has been regressed onto the EPC and it is shown in figure 7. The projection has been done for different lags (lagging the SSH field from –25 days to +25 days) to show the time evolution over the whole TA as the wave is propagating. The projection shows very clear spatial structure for the beginning of the downwelling (upwelling) equatorial Kelvin wave at the western equator at lag -15 (lag +15). The Kelvin wave propagates equatorially trapped at lag +5 (lag -25) reaching the African coast at lag +25 (lag -5). At the Guinean Dome and 5°S, it is visible a

Rossby wave-like radiation propagating westward al lag -15 (lag +15). Finally, the coastally trapped Kelvin wave propagates as far as ~15 degrees of latitude at lag -25 (lag +5).

The EEOF analysis has discriminated a very robust propagating pattern associated with equatorial and coastally trapped Kelvin wave. We have evidenced the importance of the intraseasonal propagating signals, and particularly in boreal autumn-winter, with different methodologies. The fact that Kelvin wave appears as a mode achieves the importance of the waves in the context of the TA variability. The EEOF information will be used in the second part of the paper to study the associated air-sea interactions.

6 Finer estimates of propagation phase speed and teleconnections

Once the intraseasonal climatology and the leading boreal autumn-winter mode are underlined, it is worth coming back to the intraseasonal timeseries through a lead-lag correlation analysis. It allows for both, a finer quantification of the phase speed and the teleconnections sustained by the waves.

6.1 Propagation phase speed

The speed of oceanic wave propagation is important in determining the oceanic response time to disturbances from the equilibrium state. A thorough estimate offers also a sound way to evidence the wave nature of the apparent propagations in the band-pass filtered data. The equatorial Kelvin wave has a phase speed defined by the linear theory as:

$$c_n = (gh_n)^{1/2}$$

where h_n is the equivalent depth for each n mode. The Atlantic equatorial Kelvin wave propagations have been shown in observational data and linear theory to have a phase speed range 2.4-2.9 m/s phase speed for the first baroclinic mode, 1.2-1.5 m/s for the second mode and 0.8-1 m/s for the third mode (du Penhoat and Treguier, 1985; Philander, 1990; Katz, 1997; França et al, 2003; Illig et al., 2004; Guiavarc'h et al., 2008).

Figure 8 shows the one point lag correlation for the intraseasonal climatology shown in figure 5, at 99% confidence level, for the modelled (top panel) and the observed (bottom panel) SSH and z18 variables. We have chosen four different points along the north (figure 8a) and south (figure 8b) wave-track corresponding to different regions; eastern equator, GG, southern African coast, and subtropical regions. The lag correlation for the z18 is also shown in contours, giving a similar phase speed than the one from the SSH. At the subtropics (i.e. the 220-260 north track-points and the 160-190 south track-points), the slope tends towards zero as the SSH signal shows nearly horizontal structure poleward of ~12 degrees latitude for both model and observations (as shown in figures 4a, 5a and 6).

The phase speed can be easily computed by linear regression of the maximum correlations at each point and lag in figure 8. The different linear fittings corresponding to 2.5, 1.8 and 1.5 m/s are included in figure 8. The visual comparison with the arrows indicate that the observed climatological Kelvin wave phase speed is ranging from 1.5 to 2 m/s. Due to the large dispersion of the data in the lag correlation plots, we have also computed the phase speed with Radon Transform (RT) methodology, which is a more accurate technique. The RT is very useful image processing technique for the satellite images, and it has been used before to characterize the phase speed of the oceanic Rossby waves (Chelton and Schlax, 1996; Polito and Cornillion, 1997; Hill et al., 2000;

Challenor et al., 2001). To compute the RT of the track-time plot (hovmuller) for different values of direction is equivalent to compute the energy in the spectrum along lines of constant speed, and it is the most straightforward method to find the value of the speed for which that energy is maximum (Challenor et al., 2001). The corresponding angle of the maximum RT standard deviation is defined as the angle of the propagation. The methodology has been applied following the Hill et al.'s work (2000), for the observed and modelled SSH hovmuller, for the north and the south wave-track in the entire 1993-2000 period (table 1). The phase speed calculated by RT, in average, does not change significantly the phase speed calculated by linear regression of the maximum lag correlation. The propagation phase speed ranges from 1.5 to 2.1 m/s, which is also found by other authors (Katz, 1997; França et al., 2003), and it could corresponds to a mix between the first and the second theoretical Kelvin baroclinic modes, or a modulation of the first baroclinic Kelvin wave mode speed by the first baroclinic Rossby wave mode. In addition, topography effects, stratification changes and the beers of modes can intricately be disturbing the measurements. It is important to notice that performing the RT for each point results in important variations along the tracks (not shown), especially from the equator to the coast, which can be also observed from figures 4a, 5a and 8. The differences between the observed and the theoretical phase speed, as well as the speed variations along the wave-track will need further investigations.

Nevertheless, the velocities found for both, north and south wave-tracks, for the modelled and the observed SSH and with different methods show a satisfactory agreement of the model with the satellite estimates (table 1). This means that, even with a low resolution, the model is suitable to study oceanic Kelvin wave propagations, at least equatorward of about 12 degrees of latitude. Overall, the amplitude (figure 4b, and

5a) and the phase speed (figure 8), are both important wave factors and are well reproduced by the OGCM simulation. This result will be important in order to diagnose the forcing mechanisms in the second part of this study.

From the calculated phase speed, we can conclude that the Kelvin wave propagation seen in figures 4, 5 and 6, is expressing mainly the first two baroclinic Kelvin wave modes along the equator and the African coast.

6.2 How far Kelvin wave travels? Evidence for teleconnections

Figure 8 can also be used to quantify how SSH intraseasonal variability along the coast and as far as about 12 degrees (around 200 north track-point and 150 south track-point) is remotely controlled by the wave propagating signal.

In these plots, we consider that the teleconnection breaks down where the apparent slope changes drastically, in particular where it becomes more horizontal. Although, as further away from each point smaller is the lag correlation with the point, and the propagation direction is difficult to discern due to the large physical processes implied, it can be seen equatorial connection driving SSH anomalies along the coastal track. Hence, starting with the northern coastline, the correlation centered at 5°W-0°N (90 track-point) shows continuity from the equator to the coast, although there is a change in the slope at the coast of the GG as noted previously (~120 track-point, transition between the equatorial and coastal wave-guide), and the slope break latitude is reached at about 10N (195 track-point) with a correlation of about 0.4. It suggests that this equatorial point still remotely controls 16% of the intraseasonal variance at ~10°N. The correlations centred at 3°E over the GG (140 north track-point) indicate, as expected, a clear control from the eastern equator, as well as a significant impact in the propagation direction up to ~16°W;10°N (195 north track-point) in the observations, and further poleward in the model. At these latitudes, the explained variance drops down to about 10-20%. In the third panel, centered at 14°W-8°N (190 track-point) the correlations for the observations show that the point is partly controlled by locations behind, but no signal seems to propagate further north. Beyond 12°N (figure 8a, 215 track-point), the SSH is more related to neighbouring points at lag zero, suggesting other type of coherent local forcing.

For the south (figure 8b), the correlation shows even more continuity between the equator and the coast than for the north, probably due to the more straight coastline. The correlation slope appears to break in the vicinity of 12°S (150 track-point). Beyond this point the correlation is significant but the slope is not coherent with a teleconnection via Kelvin wave propagations and suggests a control by other processes. The lack of propagation beyond 12°S is seen clearer for z18 (figure 8b-top 175 track-point), while the observed SSH (figure 8b-bottom 175 track-point) shows more correlation with the equatorial points.

In conclusion, the T/P SSH support the importance of teleconnection through Kelvin waves along the tropical African coast, from the equator up to 12°S and 10°N (12°N in the model). These latitudinal teleconnection thresholds could be due, in part, to the limits of the data resolution relative to the Rossby radius of deformation (close to 15 degrees of latitude). They are likely as well associated with the location of the intense coastal Mauritanian/Senegal and Angola/Benguela upwelling systems. Roughly, it is in the vicinity of 10 degrees of latitude, depending on the season, where the isopycnal surfaces start to outcrop in these upwelling regions. Hence, the signals carried out by the waves are partly transferred into the mixed layer, and correspondingly limit the ability of the waves to propagate information.

In practice, because the dissipative effects, there should be a limit to the distance to which the information is carried poleward by waves (Gill, 1982; Clarke and Shi, 1991). The lack of correlation at higher latitudes could be because of a great deal of energy is also found in smaller-scale motions; these may be eddies, wave motions due to small-scale features by bottom topography or loss of energy by Rossby waves radiation from the African coast (Mittelstaedt, 1991). At last, the orientation relative to the coast, the regularity and intensity of the trade winds exhibit major changes between the deep tropics, equatorward of 10°N, and the tropical-subtropical regions. We will show in the second part of this study that, the SSH variability poleward of 12 degrees of latitude is essentially controlled by local wind to the expense of teleconnection processes.

7 Conclusions

This paper is an attempt to provide new and sound insights into TA intraseasonal Kelvin wave activity. This topic has been little considered in comparison with the Pacific basin (Kessler et al., 1995; Cravatte et al., 2003; Roundy and Kiladis, 2006). It is essential to investigate it thoroughly, in light of the recent Aviso T/P dataset and state of the art OGCM, considering how often is remote forcing by Kelvin waves invoked to interpret TA variability, particularly in the vicinity of the Angola/Benguela upwelling system (Florenchie et al., 2003; Rouault et al., 2007), as well as in the coast of the GG (Servain et al., 1982; Picaut, 1983; Aman et al., 2007).

In order to study the SSH intraseasonal variability, we have band-pass filtered the data in the 25-95 day period, emphasizing the relative active 50 day period. This processing, frequently used along the equator, enlightens here the propagation of Kelvin wave signals polewards along the African coast. In the present part of this study, we demonstrate the possibility of visualizing equator to coast propagations of observed and modelled SSH and thermocline intraseasonal anomalies over several years in the TA. The TOPEX/Poseidon and 0.5° resolution OGCM simulation datasets have proved to be suitable for the identification and characterization of equatorial Kelvin waves and their continuity within the tropical band as coastally trapped Kelvin waves at intraseasonal frequencies. Such signals can clearly be followed over distance of thousands of kilometres along the coasts, especially equatorward of 10 to 15 degrees of latitude. However, the filter reduces the variance of the total signal by about a factor of two, down to one centimetre at the equator and two along the coast.

The estimated propagation phase speeds are found to be in the range between the first and second theoretical Kelvin baroclinic modes (from 1.4 m/s to 2.6 m/s). The results are homogenous for the observed and modelled SSH, for the northern and the southern wave-tracks, and from the different methodologies (RT and linear regression). Nevertheless, a finer understanding of the phase speeds and the thermocline response would require a modal analysis along the coast.

In addition, lag correlation plots allowed for the quantification of the remote effects of the waves along the coast. It is possible to state that the eastern equator SSH can explain about 25% of the intraseasonal variability of the GG so-called coastal upwelling and 16% of the intraseasonal variability of the Benguela upwelling. Although the SSH variability over the Mauritanian/Senegal upwelling region is less influenced by the wave propagations, the results support the existence of a remote forcing via eastward and poleward intraseasonal Kelvin waves of the lowest latitudes of the north and south eastern tropical upwellings.

The major result of our study is the demonstration that it is possible and useful to simplify the complex intraseasonal activity down to two synthetic signals; an intraseasonal climatology and an Extended EOF mode. From the intraseasonal climatology, a particularly striking result is that major Kelvin wave activity occurs with a high degree of recurrence in boreal autumn-winter season (September-December downwelling and November-January upwelling Kelvin waves). The model simulation helped to quantify the associated stratification changes, which are very well correlated and reach a few meters for a few centimers surface signals. The most robust continuity develops in early boreal winter from the west equator eastward and poleward towards the Benguela upwelling system and the coast of the GG in late boreal winter, in observed and modelled SSH (figure 5a) as well as within the thermocline (figure 5c).The connecting signals propagation velocity, ~1.8 m/s, supports the existence of some remote forcing via Kelvin waves.

The extended EOF mode for this boreal autumn-winter Kelvin wave propagation is the second synthetic view of this phenomenon. The mode, albeit of weak amplitude, provides an associated spatial structure that proves well the Kelvin wave nature of these teleconnections. The fact that Kelvin wave appears as a mode achieves the importance of the waves in the context of the TA SSH variability. Its principal component timeseries can be used to identify interannual modulations, as well as construct through regression associated signals in pertinent variables, such as the wind stress and SST, which will be presented in the second part of the study.

In order to develop a detailed description of SSH propagations and coastal teleconnections in this paper, we have left aside the analysis of the complementary process controlling the SSH: the local atmospheric forcing. In the second part of this study, we will focus on the causes for the equatorial Kelvin wave triggering at the western equatorial Atlantic, its relationship with the atmosphere, the possible impacts on the SST and the particular behaviour in the subtropics.

Acknowledgements: We would like to thank to the editor Raghu Murtugudde and anonymous reviewers for their helpful comments on the manuscript. We are grateful to Christian Ethe and Gurvan Madec for kindly providing the model run outputs, and Gildas Mainsant for his help in the analysis. We also thank Serge Janicot, Vincent Echevin and Frédéric Vivier for stimulating discussions. This study has been supported by ANETUS (CNES/NASA) and the Spanish MCYT CGL2006-04471 and REN2002-03424 programs, which has also funded Irene Polo and her research stage at LOCEAN laboratory as part as her phD thesis.

References

Adamec, D., and J. J. O'Brien (1978), The Seasonal Upwelling in the Gulf of Guinea Due to Remote Forcing, *J. Physical Oceanog.*, 8, 1050-1060.

Aman, A., L. Testut, P. Woodworth, T. Aarup, and D. Dixon (2007), Sesonal Sea Level Variability in the Gulf of Guinea from altimetry and tide gauge. Submitted.

Arnault, S., Y. Menard, and J. Merle (1990), Observing the tropical Atlantic Ocean in 1986--1987 from altimetry, *J. Geophys. Res., 95* (C10), doi: 10.1029/90JC00347.

Arnault, S., L. Gourdeau, and Y. Menard (1992), Comparison of the altimetric signal with in-situ measurements in the tropical Atlantic ocean, *Deep Sea Res*., *39*(3/4), 481-499, 1992.

Arnault, S., and R. E. Cheney (1994), Tropical Atlantic sea-level variability from Geosat (1985-1989), *J. Geophys. Res., 99*, 18207-18223.

Arnault, S., and C. Le Provost (1997), Regional identification in the tropical Atlantic Ocean of residual tide errors from an empirical orthogonal function analysis of TOPEX/POSEIDON altimetric data, *J. Geophys. Res*., *102*, 21022-21036.

Berliand, M. E., and T. G. Strokina (1980), Global distribution of the total amount of clouds, *Hydrometeorological Publishing House*, Leningrad, Russia, 71 pp.

Carton, J. A., X. H. Cao, B. S. Giese, and A. M. daSilva (1996), Decadal and interannual SST variability in the tropical Atlantic Ocean, *J. Phys. Oceanogr., 26*, 1165-1175.

Challenor, P.G., P. Cipollini, and D. Cromwell (2001), Use of the 3D radon transform to examine the properties of oceanic Rossby waves, *J. Atmos. Oceanic Technol., 18(9),* 1558-1566.

Chelton, D. B., and M. G. Schlax (1996), Global observations of oceanic Rossby waves, *Science*, *272*, 234-238.

Clarke, A. J. (1978) , On the generation of the seasonal coastal upwelling in the Gulf of Guinea, *J. Geophys. Res.,* 84, 3743-3751.

Clarke, A. J. (1983), The Reflection of Equatorial Waves from Oceanic Boundaries, *J. Phys. Oceanogr., 13*, 1193-1207.

Clarke, A. J., and C. Shi (1991), Critical frequencies at ocean boundaries, *J. Geophys. Res., 96*, 10 731–10 738.

Cravatte S., J. Picaut and G. Eldin (2003), Second and first Kelvin modes in the equatorial Pacific at intraseasonal timescales, *J. Geophys.Res.*, *108*, doi:10.1029/2002JC001511.2003.

de Boyer-Montégut, C., J. Vialard, S. S. C. Shenoi, D. Shankar, F. Durand, C. Ethé, and G. Madec (2007), Simulated seasonal and interannual variability of mixed layer heat budget in the northern Indian Ocean, *J. Climate*, 20, 3249-3268

du Penhoat, Y., and A.-M. Treguier (1985), The seasonal linear response of the Atlantic Ocean, *J. Phys. Oceanogr*., *15*, 316-329.

Florenchie, P., J. R. E. Lutjeharms, C. J. C. Reason, S. Masson, and M. Rouault (2003), The source of Benguela Niños in the South Atlantic Ocean, *Geophys. Res. Lett*., vol 30, no 10, 1505.

França, C., I. Wainer, A. R. De Mesquita, and G. J. Goni (2003), Planetary equatorial trapped waves in the Atlantic Ocean from TOPEX/Poseidon altimetry, *in*: Goni, G.J.; Malanotte-Rizzoli, P. (Ed.) (2003). *Interhemispheric water exchange in the Atlantic Ocean. Elsevier Oceanography Series, 68,* 213-232.

Fraedrich, K., J. L. McBride, W. M. Frank, and R. Wang (1997), Extended EOF Analysis of Tropical Disturbances: TOGA COARE, *J. Atmos. Sci*, *54*, 19, 2363–2372.

Gill, A. E. (1982), *Atmosphere-Ocean Dynamics*, Academic Press. 662 pp. ISBN 0122835220.

Greatbatch, R. J. and K. A. Peterson (1996), Interdecadal variability and oceanic thermohaline adjustment, *J. Geophys. Res., 101*, 20467–20482.

Grodsky, S.A., and J.A. Carton (2006), Influence of the tropics on the climate of the South Atlantic, *Geophys. Res. Letts.*, Art. No. L06719.

Guiavarc'h, C., A. M. Treguier, A. Vangriesheim (2008), Remotely forced biweekly deep oscillations on the continental slope of the Gulf of Guinea, *J. Geosphys. Res*., in press.

Han, W., P.J. Webster, J. Lin, W.T. Liu, R. Fu, D. Yuan, and A. Hu (2008), Dynamics of intraseasonal sea level and thermocline variability in the equatorial Atlantic during 2002-2003*, J. Phys. Oceanogr*., in press

Handoh, I. C. and G. R. Bigg (2000), A self-sustaining climate mode in the Tropical Atlantic, 1995-97: Observations and modelling, *Q JR. Meteo. Soc., 126*, 807-821.

Hendon, H. H., B. Liebmann, and J. D. Glick (1998), Oceanic Kelvin Waves and the Madden-Julian Oscillation, *J. Atmos. Sci., 55*, 88-101.

Hill, K. L., I. S. Robinson, and P. Cipollini (2000), Propagation characteristics of extratropical planetary waves observed in the ATSR global sea surface temperature record, *J. Geophys. Res., 105*(C9), 21927-21945.

Hormazabal, S., G. Shaffer and O. Pizarro (2002), Tropical Pacific control of intraseasonal oscillations off Chile by way of oceanic and atmospheric pathways, *Geophys. Res. Lett*., *29*, doi: 10.1029/2001GL013481.

Illig S., D. Gushchina, B. Dewitte, N. Ayoub, and Y. du Penhoat (2006), The 1996 equatorial Atlantic warm event: Origin and mechanisms, *Geophys. Res. Lett*., 33, doi: 10.1029/2005GL025632.

Illig S., B. Dewitte, N. Ayoub, Y. du Penhoat, G. Reverdin, P. De Mey, F. Bonjean, and G. S. Lagerloef (2004), Interannual long equatorial waves in the tropical Atlantic form a high resolution ocean general circulation model experiment in 1981-2000, *J. Geophys. Res.*, *109*, C02022, doi. 101029/2003JC001771.

Jacobs, G.A., H. E. Hurlburt, J. C. Kindle, E. J. Metzger, J. L. Mitchell, W. J. Teague, and A. J. Wallcraft (1994), Decade-scale trans-Pacific propagation and warming effects of an El Niño anomaly, *Nature, 370*, 360-363.

Kalnay, E. and co-authors (1996): The NCEP/NCAR 40-year Reanalysis Project. *Bull Amer. Meteor. Soc.*, 77, 437-471.

Katz, E.J. (1997), Waves along the equator in the Atlantic, *J. Phys. Oceanogr.*, *27*, 2536–2544.

Kessler, WS, MJ McPhaden, and KM Weickmann (1995), Forcing of intraseasonal Kelvin waves in the equatorial Pacific, *J. Geophys. Res., 100*, 10613-10631.

Levitus, S. (1998), Climatological Atlas of the world ocean. *Tech. Rep. 13*, NOAA, Rockville, Md.

Madec, G., P. Delecluse, M. Imbard, and C. Lévy (1998), OPA 8.1 Ocean General Circulation Model reference manual. *Note du Pôle de modélisation*, Institut Pierre-Simon Laplace, N°11, 91 pp.

Matsuno, T. (1966), Quasi-geostrophic motions in the equatorial area, *J. Met. Soc. Japan*, *44*, 25–43.

Mayer, D. A., R. L. Molinari, M. O. Baringer, and G. J. Goni (2001), Transition regions and their role in the relationship between sea surface height and subsurface temperature structure in the Atlantic Ocean, *Geophys. Res. Lett.,* 28, 3943–3946.

Meyers, S. D., A. Melsom, G. T. Mitchum and J. O'Brien (1998), Detection of the fast Kelvin Wave teleconnection due to El Nino-Southern Oscillation, *J. Geophys. Res., 103*, 27655-27663.

Mittelstaedt, E. (1991), The ocean boundary along the northwest African coast: Circulation and oceanographic properties at the sea surface, *Progress in Oceanography*, *26*, 307-355.

Moore, D. W. 1968: Planetary-gravity waves in an equatorial ocean. Ph. D. thesis, Harvard University, Cambridge, Mass.

Moore, D. W., P. Hisard, J.P. McCreary, J. Merle, J. J. O'Brien, J. Picaut, J. Verstraete, and C. Wunsch (1978), Equatorial adjustment in the eastern Atlantic, *Geophys. Res. Lett.*, 5, 637-640.

O'Brien, J. J., D. Adamec, and D. W. Moore (1978), A simple model of upwelling in the Gulf of Guinea, *Geophys. Res. Lett., 5*, 8, 641-644.

Philander, S. G. H. (1990), *El Niño, La Niña, and the Southern Oscillation.*International Geophysics Series, Vol. 46, Academic Press, 293 pp.

Picaut, J. (1983), Propagation of the seasonal upwelling in the eastern equatorial Atlantic, *J. Phys. Oceanogr., 13*, 18-37.

Polito, P. S., and P. Cornillon (1997), Long baroclinic Rossby waves detected by TOPEX/POSEIDON, *J. Geophys. Res.*, *102*, 3215-3235.

Rebert, J., J. Donguy, G. Eldin, and K. Wyrtki (1985), Relations between sea level, thermocline depth, heat content, and dynamic height in the tropical Pacific Ocean, *J. Geophys. Res.*, *90*, 11719–11725.

Rodriguez-Fonseca, B., I. Polo, E. Serrano, and M. Castro (2006), Evaluation of the north Atlantic SST forcing on the European and northern African winter climate, *Int. J.* Climatology., 25, doi: 10.1002/7joc.1234.

Rouault, M., S. Illig, C. Bartholomae, C. J. C. Reason, and A. Bentamy (2007), Propagation and origin of warm anomalies in the Angola Benguela upwelling system in 2001, *J. Mar. Sys.,* doi: 10.1016/j.jmarsys.2006.11.010.

Roundy, P. E., and G. N. Kiladis (2006), Observed Relationships between Oceanic Kelvin Waves and Atmospheric Forcing, *J. Climate, 19*, 5253-5271.

Saravanan, R., and P. Chang (2000), Interaction between tropical Atlantic variability and El Niño–Southern Oscillation, *J. Climate, 13*, 2177–2194.

Servain, J., J. Picaut, and J. Merle (1982), Evidence of Remote Forcing in the Equatorial Atlantic Ocean, *J. Phys. Oceanogr.,*12, 457-463.

Schouten, M. W., R. P. Matano, and T. P. Strub (2005), A description of the seasonal cycle of the equatorial Atlantic from altimeter data, *Deep Sea Res*., *52*, 477-493.

Stammer, D. (1997), Global Characteristics of Ocean Variability Estimated from Regional TOPEX/POSEIDON Altimeter Measurements, *J. Phys. Oceanogr., 27,* 1743-1769.

Sutton, R. T., S. P. Jewson, and D. P. Rowell (2000), The elements of climate variability in the tropical Atlantic region, *J. Climate, 13,* 3261–3284.

Trenberth, K. E., J. G. Olson, and W. G. Large (1989), A global ocean wind stress climatology based on the ECMWF analyses. National Center for Atmospheric Research, NCAR/TN-338+STR, Boulder, Colorado, 93 pp.

UNESCO (Ed.) (1996), Discharge of selected rivers of the world. Volume II (Part II), UNESCO Publishing.

Vega, A., Y. Du-Penhoat, B. Dewitte, and O. Pizarro (2003), Equatorial forcing of interannual Rossby waves in the eastern South Pacific, *Geophys. Res. Lett*., *30*, 5, 1197.

Weare, B. C., and J. S. Nasstrom (1982), Examples of extended empirical orthogonal function analysis, *Mon. Weath. Rev., 110*, 481-485.

Wilson, C., and D. Adamec (2002), A global view of bio-physical coupling from SeaWiFS and TOPEX satellite data, 1997–2001, *Geophys. Res. Lett.*, 29, 8. 10.1029/2001GL014063.

Xie, P., and P. A. Arkin (1996), Analysis of global monthly precipitation using gauge observations, satellite estimates and numerical model predictions, *J. Climate,* 9, 840-858.

Figure captions

Figure 1(a) Seasonal cycle of the observed T/P SSH (shaded areas in cm) and the wind stress (vectors in 10^{-1} N/m^2), for the equatorial Atlantic and the northern (left) and southern (right) African coast. The wind stress is projected over virtual xy-axes, positive eastward and northward respectively.

b) Map of the Grid points along the Equator and the African coast used in the study as Kelvin wave-tracks.

Figure 2 Hovmuller diagrams for the observed SSH interannual anomalies (cm), following the track of the figure 1b, for the equator and the northern African coast (left) and the southern African coast (right), for the 1993-2000 period.

Figure 3(a) Variance-preserving spectra of observed SSH data (in cm^2). Periodicity versus track-points for the north (left panel) and south (right panel) Kelvin wave-track. Top panel corresponds to 20-500 days periodicity range, and bottom panel corresponds to 0-100 day periodicity range and (b) Power spectrum ranging from 20 to 100 days (top panel) of three points along the north wave-track corresponding to the western equator, eastern equator and Gulf of Guinea (from left to right) and the associated timeseries (bottom panel). The frequency around 50-66 days period has been remarked.

Figure 4(a) Hovmuller diagrams of the observed intraseasonal SSH (in cm), following the wave-track of figure 2, for the equator and the northern African coast (left) and the southern African coast (right), for the 1993-200 period. The filtered SSH signals are the result of applying a 21-91 day band-pass filter. The white arrows correspond to 1.8 m/s propagation phase speed.

Figure 4(b) Variance of the intraseasonal SSH anomalies for the observations (solid line) and the model (dotted line) for the north track (black lines) and the south track (grey lines) and (c) Correlation between the observed and modelled intraseasonal SSH anomalies, for the north wave-track (black-solid line) and south wave-track (grey-dotted line).

Figure 5(a) Climatology of the intraseasonal SSH anomalies (in cm) for the observations (shaded areas) and the model (contour lines, CI=0.5, the zero line has been removed), for the north wave-track (left panel) and the south wave-track (right panel). The arrows correspond to 1.8 m/s (white and black lines) and 1.6 m/s (grey line) propagation phase speeds and

Figure 5(b) Significant areas are shaded from a significance t-test, at 99% confidence level, for the correlation between the sampled average of SSH (intraseasonal climatology from figure 4a) and the temporal series for each year and for each point along the north (top panel) and the south (bottom panel) wave-tracks, for the model (left panel) and the observations (right panel).

Figure 5(c) Climatology of the intraseasonal 18°C isotherm depth anomalies (shaded areas, in m), and modelled intraseasonal SSH anomalies (contour lines, CI=0.5 cm, the zero line has been removed), for the north wave-track (left panel) and the south wave-track (right panel). The arrows correspond to 1.8 m/s propagation phase speed.

Figure 6. Leading Extended Empirical Orthogonal Function mode of the observed intraseasonal SSH along the north wave-track (top panel, in cm), and the associated Extended Principal Component for the period 1993-2001 (bottom panel) in boreal autumn-winter (September to February). The EEOF has been performed after interpolate the T/P SSH to 5-day temporal outputs and obtaining 21 lags. The white (black) arrow corresponds to 2.5 m/s (2 m/s) propagation phase speed.

Figure 7. Regression of the observed intraseasonal SSH anomalies over the whole Tropical Atlantic on the leading EEOF mode from figure 6 at different lags (shaded areas, CI=0.1 cm), only statistically significant areas at 95% confidence limit are plotted.

Figure 8(a) One point observed SSH (shaded) and modelled z18 (contour lines) intraseasonal climatology lag correlation map for several track-points for the north, and for the model (upper panel) and the observations (bottom panel). Correlation significant at the 99% confidence limit is plotted. The yellow, red and blue lines correspond to 2.5 m/s, 1.8 m/s and 1.5 m/s propagation phase speeds respectively and (b) As figure (a) but for the south African coast wave-track.

Table 1. Phase speed calculated by linear best-fitting and Radon Transform of the observed and modelled SSH of the north and south wave-tracks. The linear best-fitting has been computed and averaged from figure 8. The RT has been computed for each hovmuller for the observed (from figure 4) and modelled SSH, smoothing with at hanning window avoiding the signals around the frame. The RT of the images has been performed for the angle between -90 to 90 degrees every 0.05 degrees.

Hovmuller SSH Field	Phase speed (m/s) from linear fitting	Phase speed (m/s) from RT
Model North	1.6	1.60
Observ North	1.5	1.86
Model South	1.8	1.86
Observ South	1.9	2.10

Table 1

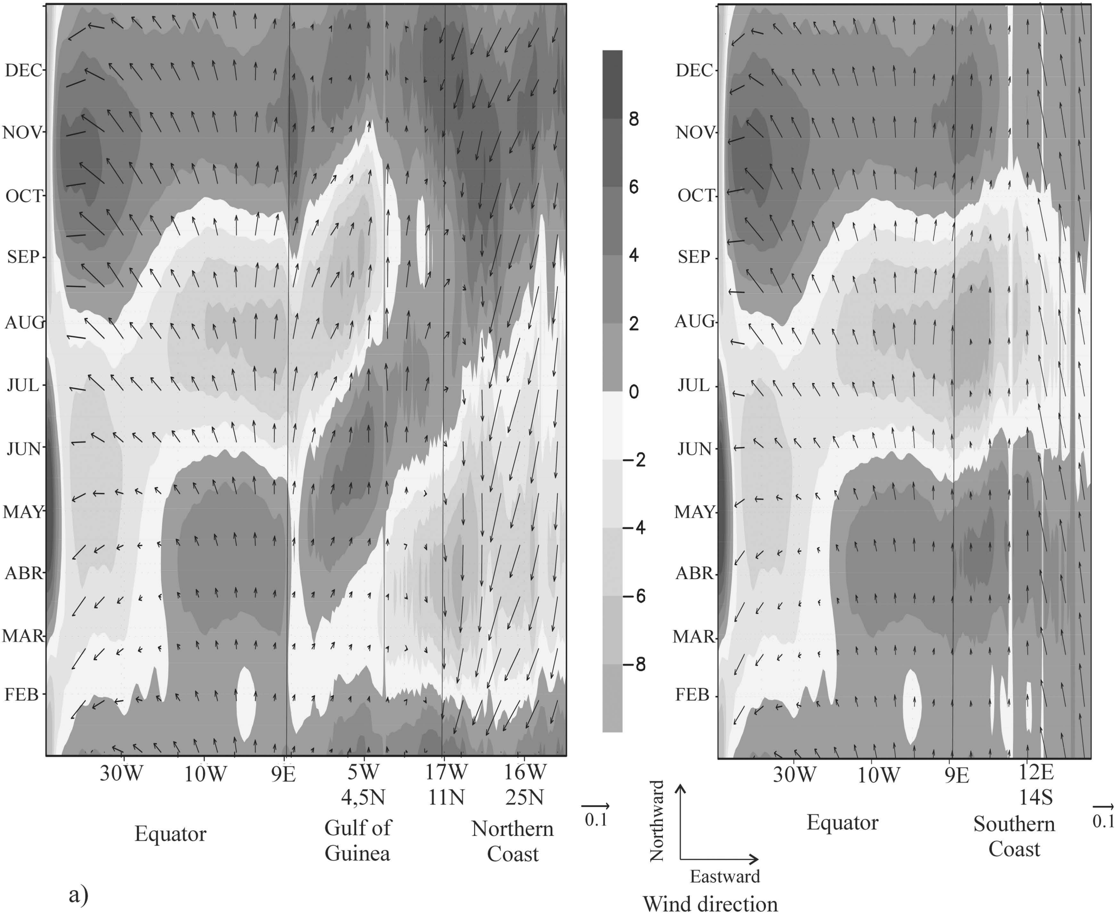
DEC
NOV
OCT
SEP
AUG
JUL
JUN
MAY
ABR
MAR
FEB
8
6
4
2
0
−2
−4
−6
−8
30W
10W
9E
5W
4,5N
17W
11N
16W
25N
0.1
Equator
Gulf of Guinea
Northern Coast
a)
Northward
Eastward
Wind direction
DEC
NOV
OCT
SEP
AUG
JUL
JUN
MAY
ABR
MAR
FEB
30W
10W
9E
12E
14S
Equator
Southern Coast
0.1

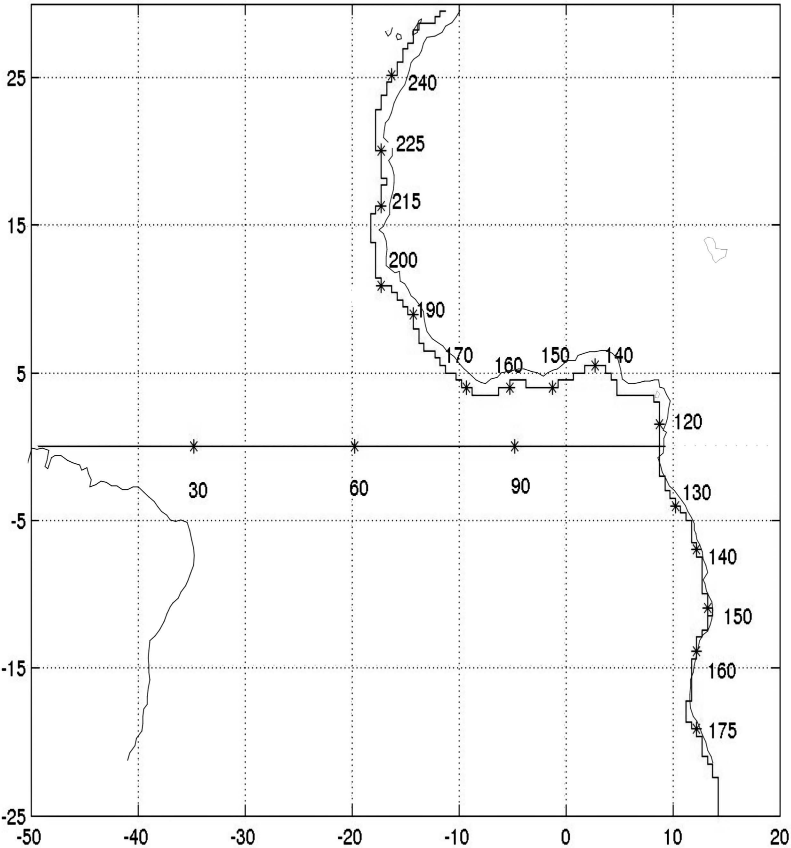
25
15
5
-5
-15
-25
-50
-40
-30
-20
-10
0
10
20
240
225
215
200
190
170
160
150
140
120
30
60
90
130
140
150
160
175

b)

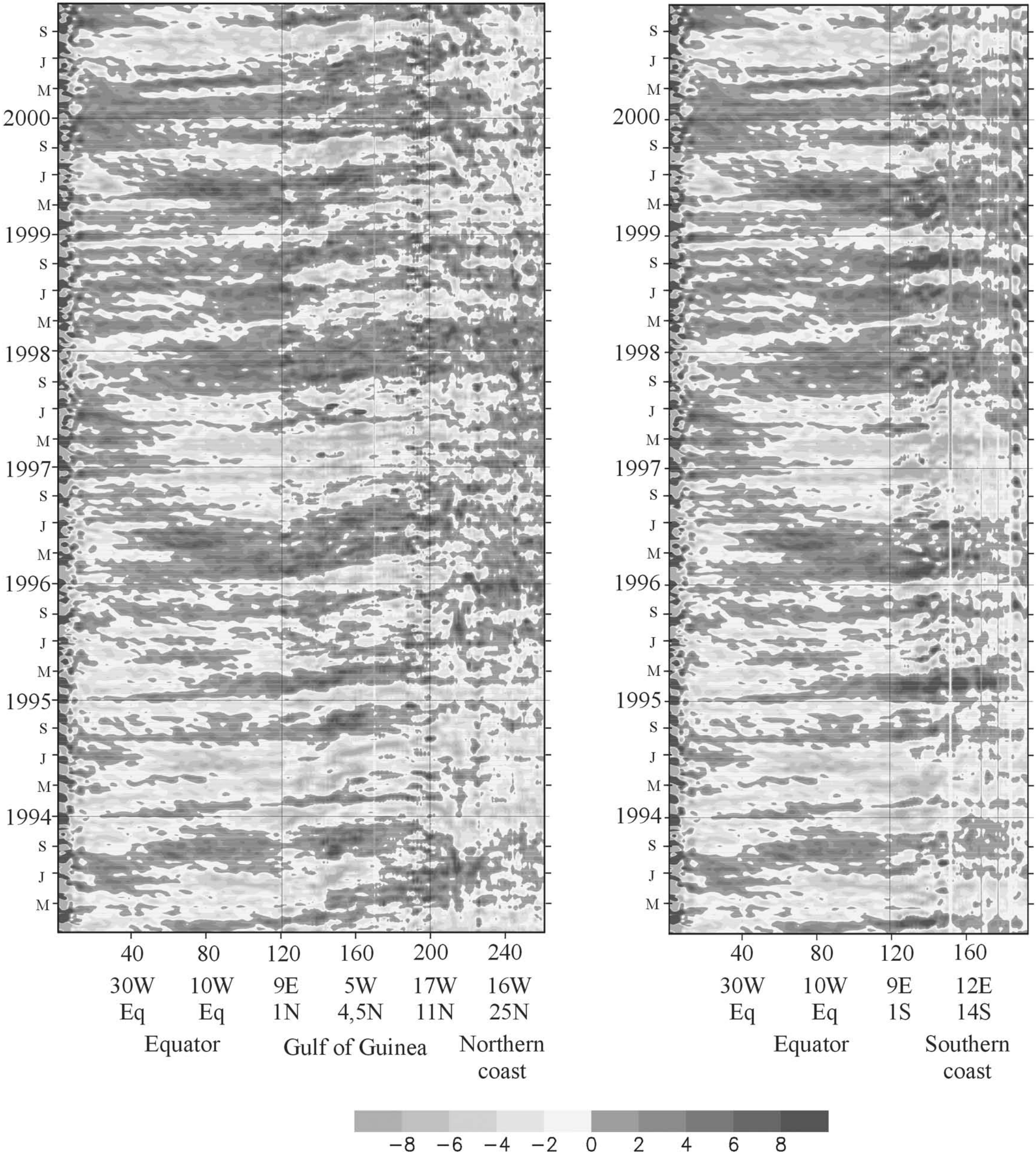
S
J
M
2000
S
J
M
1999
S
J
M
1998
S
J
M
1997
S
J
M
1996
S
J
M
1995
S
J
M
1994
S
J
M
40
80
120
160
200
240
30W Eq
10W Eq
9E 1N
5W 4,5N
17W 11N
16W 25N
Equator
Gulf of Guinea
Northern coast
40
80
120
160
30W Eq
10W Eq
9E 1S
12E 14S
Equator
Southern coast
−8
−6
−4
−2
0
2
4
6
8

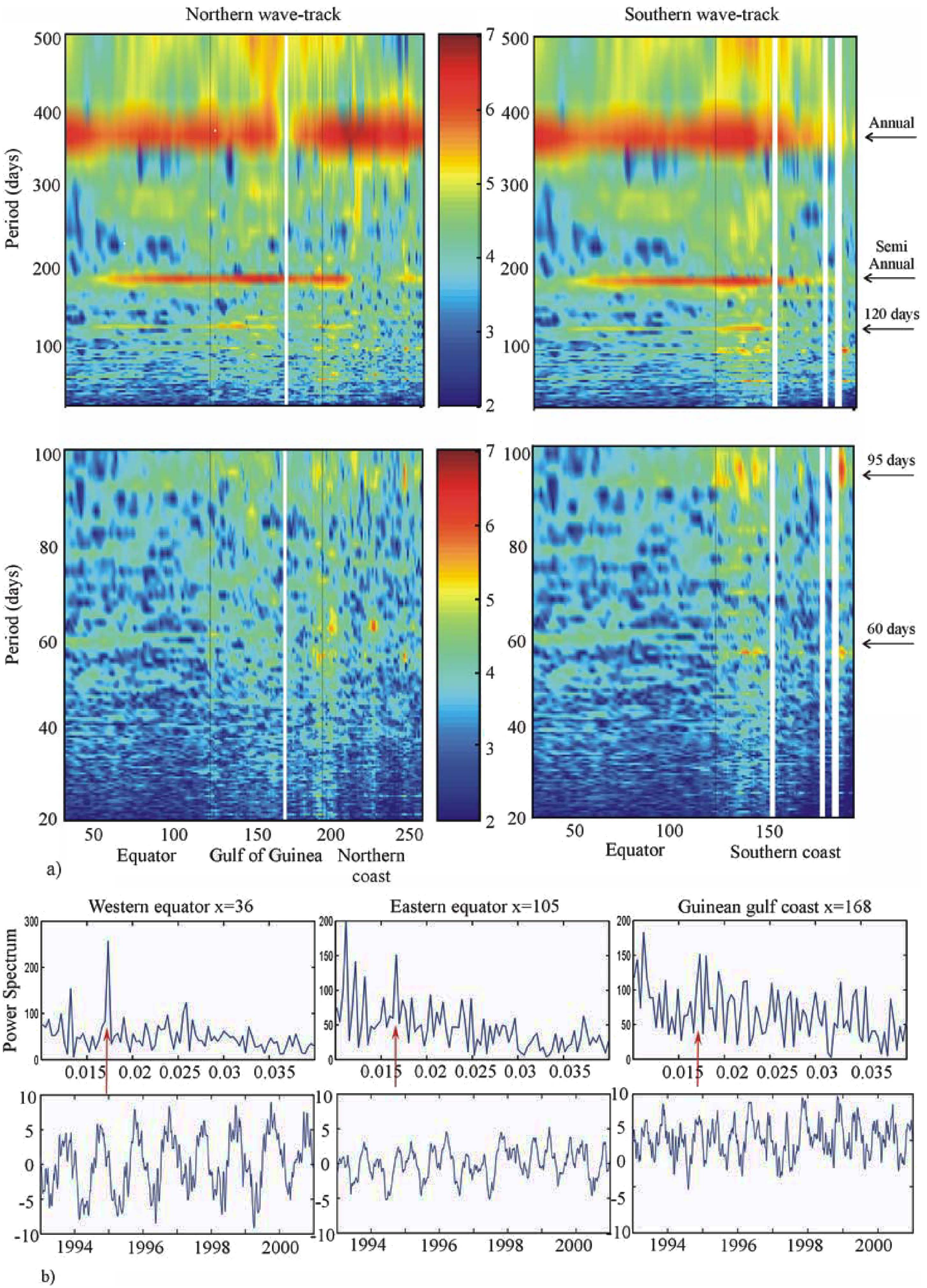
Northern wave-track
Southern wave-track
Period (days)
500
400
300
200
100
80
60
40
20
7
6
5
4
3
2
Annual
Semi Annual
120 days
95 days
60 days
50
100
150
200
250
Equator
Gulf of Guinea
Northern coast
Southern coast
a)
Western equator x=36
Eastern equator x=105
Guinean gulf coast x=168
Power Spectrum
0.015
0.02
0.025
0.03
0.035
10
5
0
-5
-10
1994
1996
1998
2000
b)

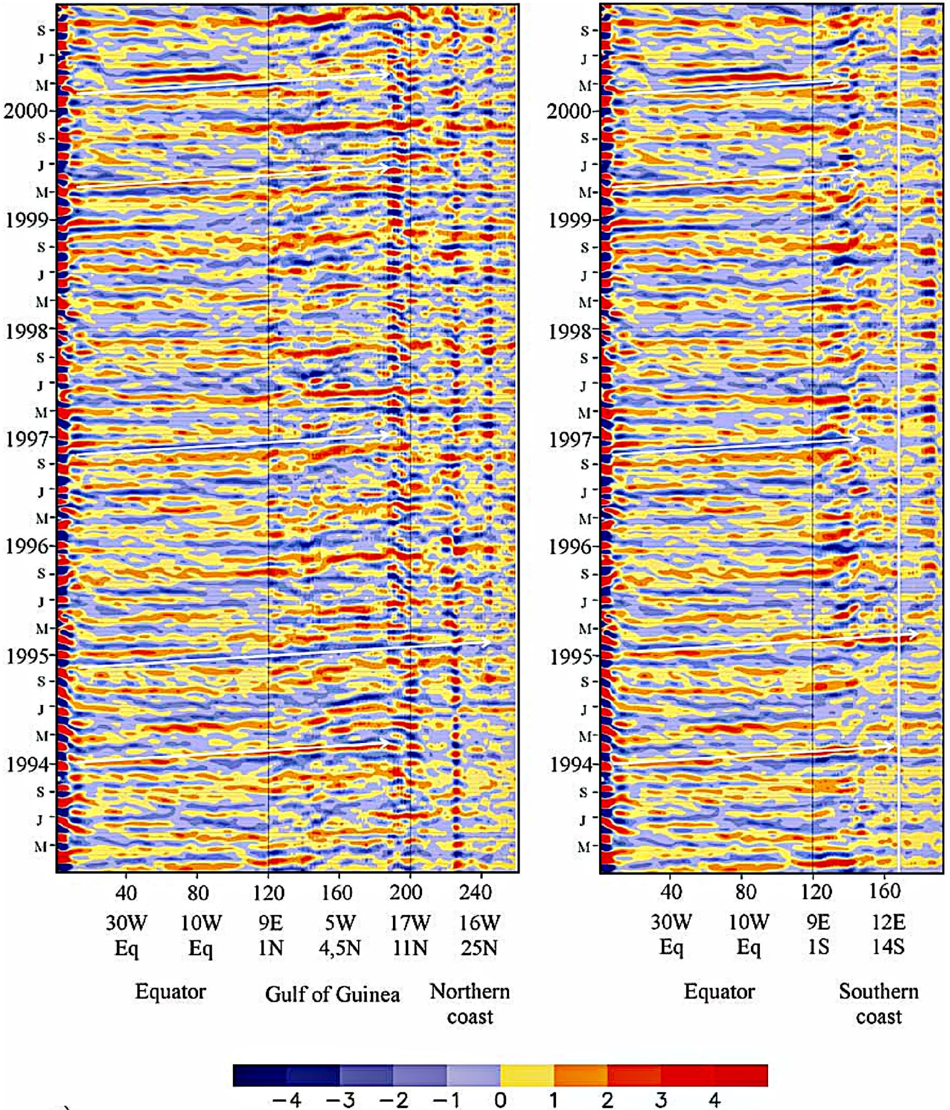
S
J
M
2000
S
J
M
1999
S
J
M
1998
S
J
M
1997
S
J
M
1996
S
J
M
1995
S
J
M
1994
S
J
M
40
80
120
160
200
240
30W Eq
10W Eq
9E 1N
5W 4,5N
17W 11N
16W 25N
Equator
Gulf of Guinea
Northern coast
S
J
M
2000
S
J
M
1999
S
J
M
1998
S
J
M
1997
S
J
M
1996
S
J
M
1995
S
J
M
1994
S
J
M
40
80
120
160
30W Eq
10W Eq
9E 1S
12E 14S
Equator
Southern coast
−4
−3
−2
−1
0
1
2
3
4

a)

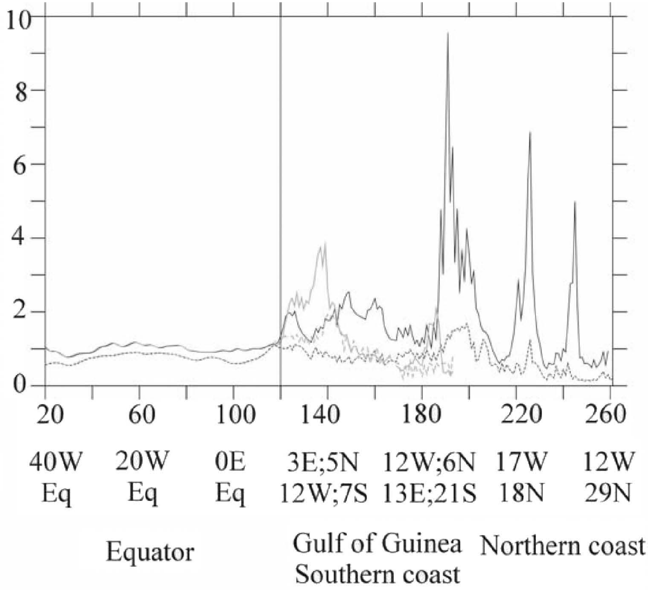
10
8
6
4
2
0
20
60
100
140
180
220
260
40W
Eq
20W
Eq
0E
Eq
3E;5N
12W;7S
12W;6N
13E;21S
17W
18N
12W
29N
Equator
Gulf of Guinea
Southern coast
Northern coast

b)

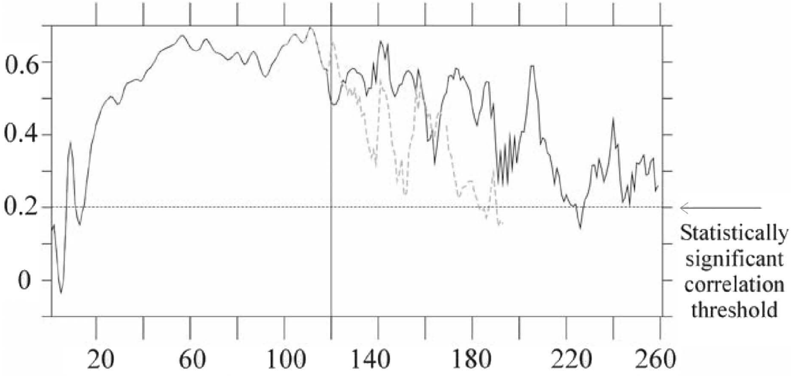
0.6
0.4
0.2
0
20
60
100
140
180
220
260
Statistically
significant
correlation
threshold

c)

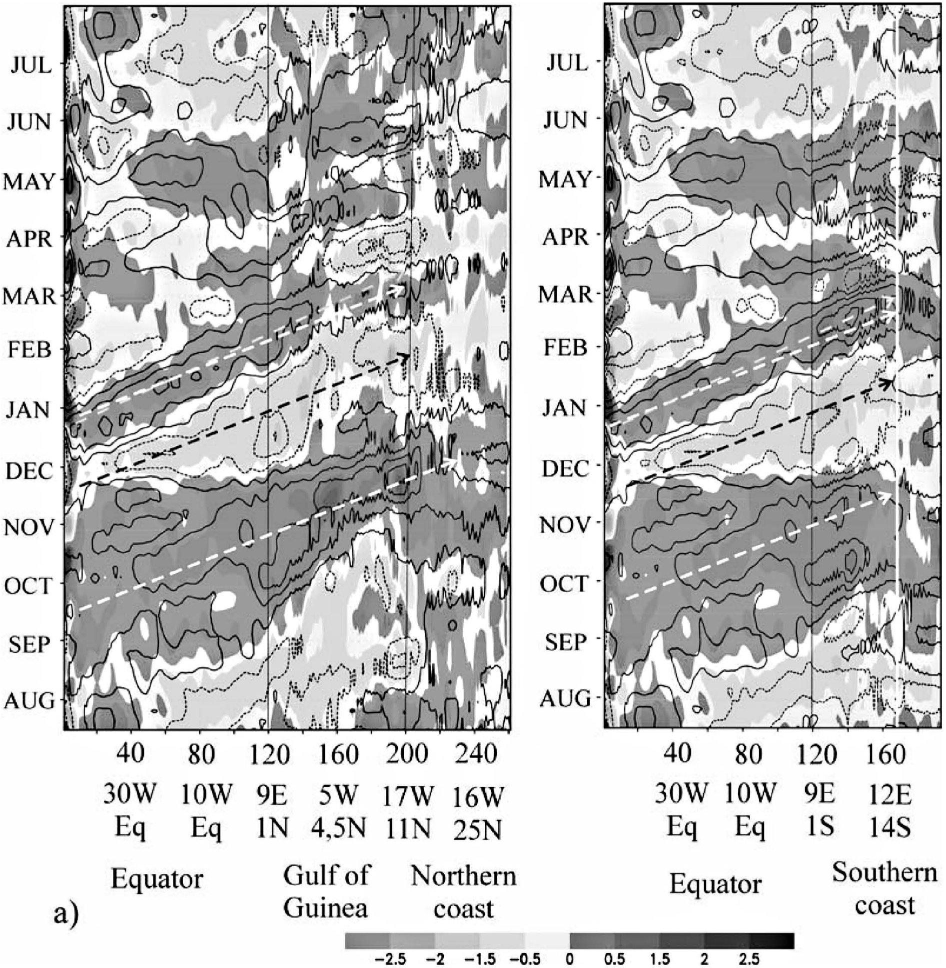
JUL
JUN
MAY
APR
MAR
FEB
JAN
DEC
NOV
OCT
SEP
AUG
40
80
120
160
200
240
30W Eq
10W Eq
9E 1N
5W 4,5N
17W 11N
16W 25N
Equator
Gulf of Guinea
Northern coast
a)
JUL
JUN
MAY
APR
MAR
FEB
JAN
DEC
NOV
OCT
SEP
AUG
40
80
120
160
30W Eq
10W Eq
9E 1S
12E 14S
Equator
Southern coast
−2.5
−2
−1.5
−0.5
0
0.5
1.5
2
2.5

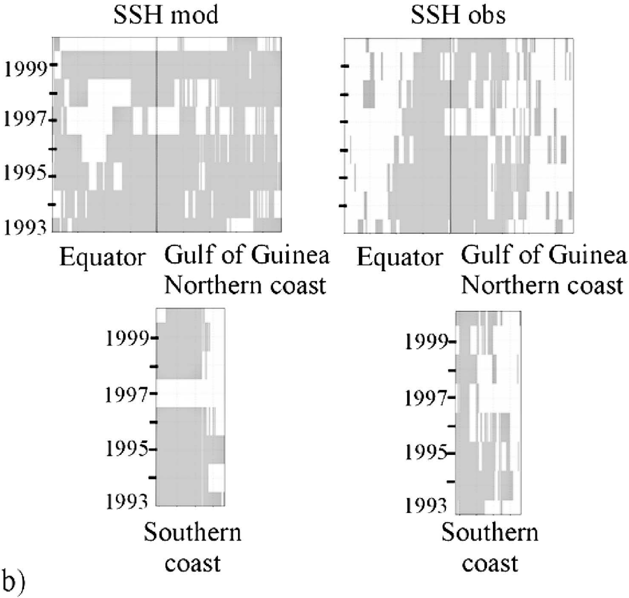
SSH mod
SSH obs
1999
1997
1995
1993
Equator
Gulf of Guinea
Northern coast
Southern
coast
b)

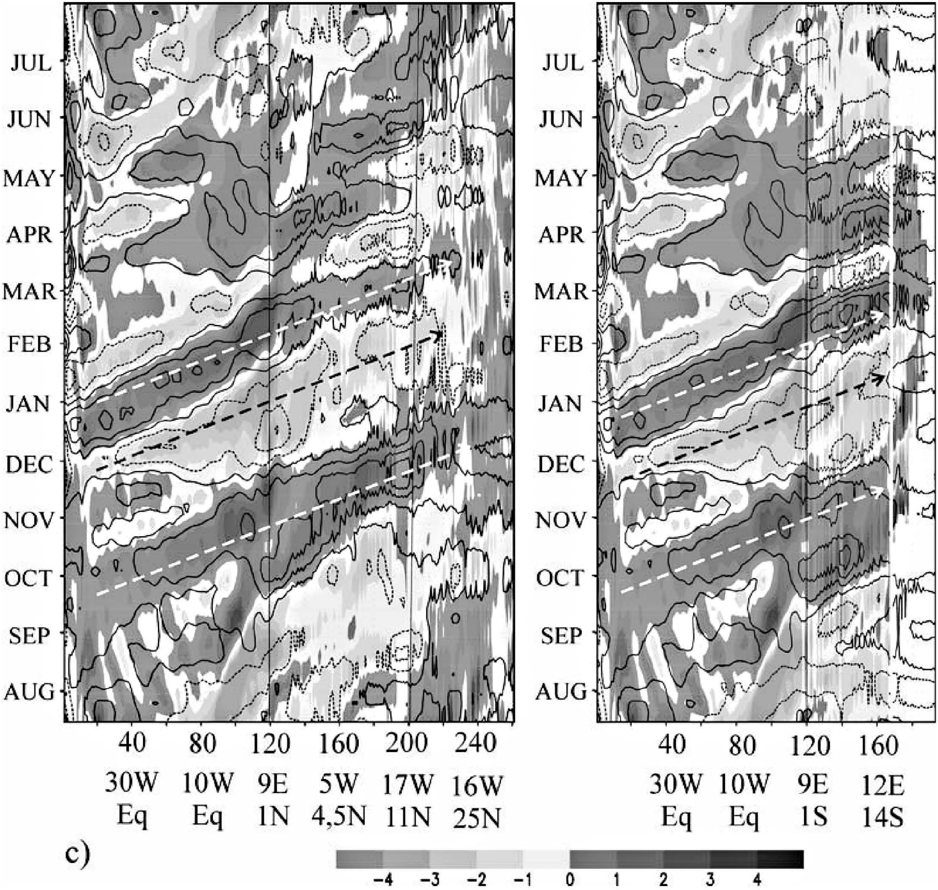
JUL
JUN
MAY
APR
MAR
FEB
JAN
DEC
NOV
OCT
SEP
AUG
40
80
120
160
200
240
30W Eq
10W Eq
9E 1N
5W 4,5N
17W 11N
16W 25N
JUL
JUN
MAY
APR
MAR
FEB
JAN
DEC
NOV
OCT
SEP
AUG
40
80
120
160
30W Eq
10W Eq
9E 1S
12E 14S
c)
−4
−3
−2
−1
0
1
2
3
4

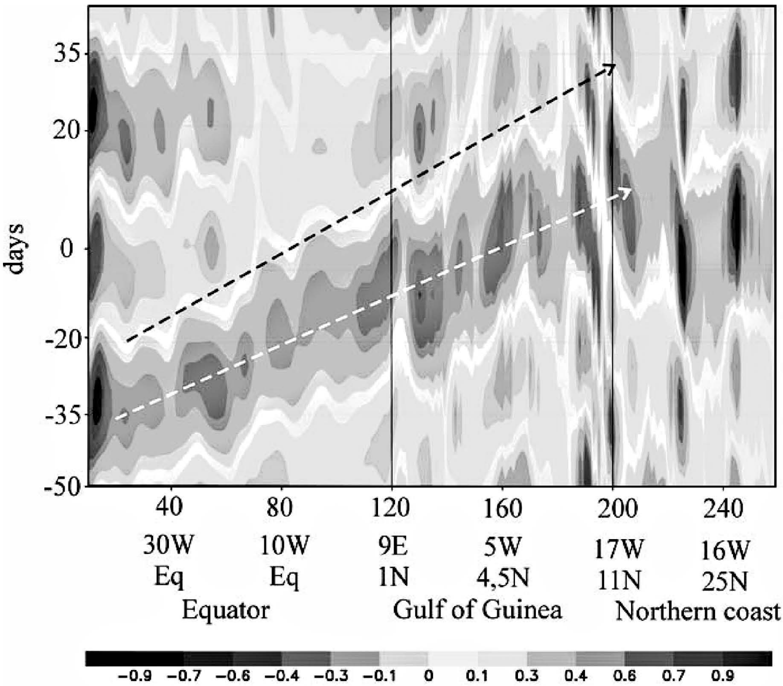
days
35
20
0
-20
-35
-50
40
80
120
160
200
240
30W
Eq
10W
Eq
9E
1N
5W
4,5N
17W
11N
16W
25N
Equator
Gulf of Guinea
Northern coast
−0.9
−0.7
−0.6
−0.4
−0.3
−0.1
0
0.1
0.3
0.4
0.6
0.7
0.9

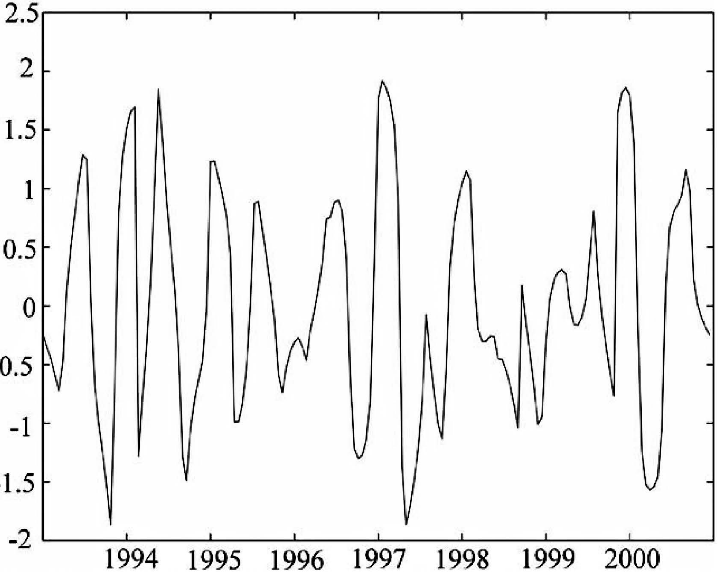
2.5
2
1.5
1
0.5
0
-0.5
-1
-1.5
-2
1994
1995
1996
1997
1998
1999
2000

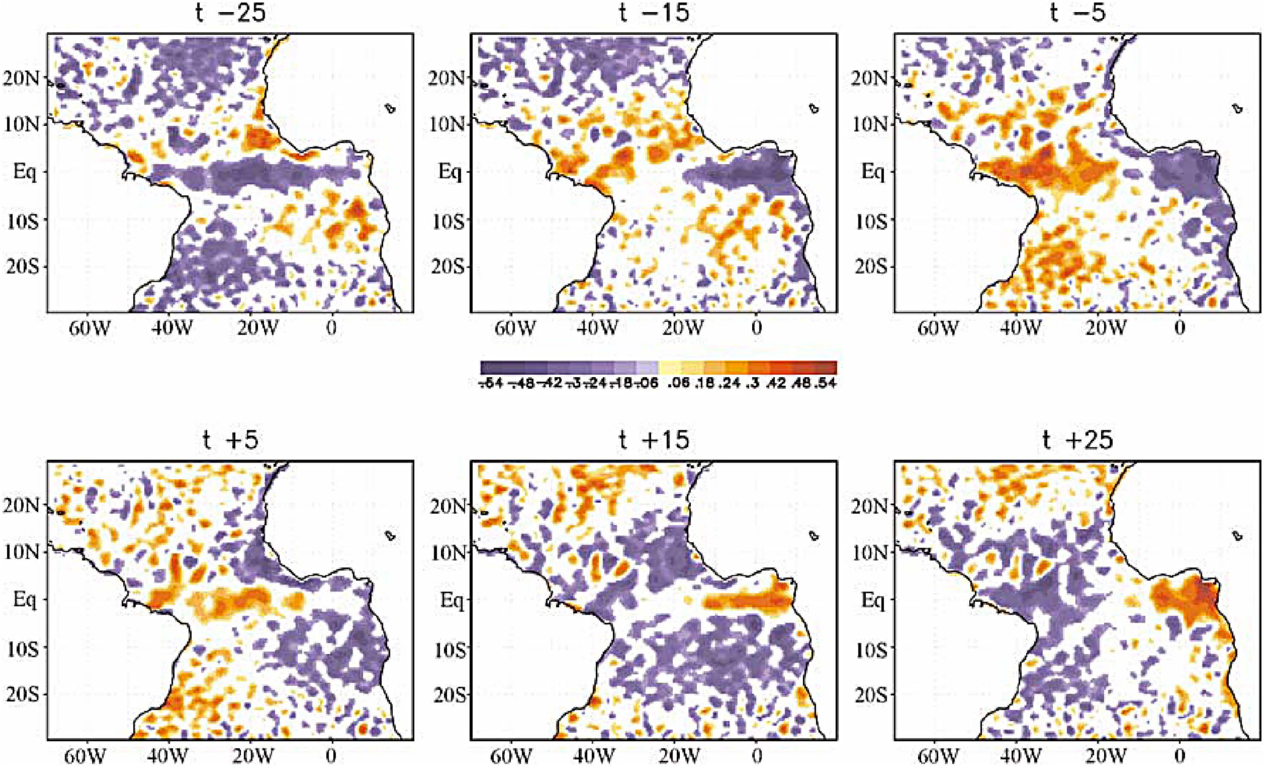
t -25
t -15
t -5
t +5
t +15
t +25
20N
10N
Eq
10S
20S
60W
40W
20W
0
-.54
-.48
-.42
-.3
-.24
-.18
-.06
.06
.18
.24
.3
.42
.48
.54

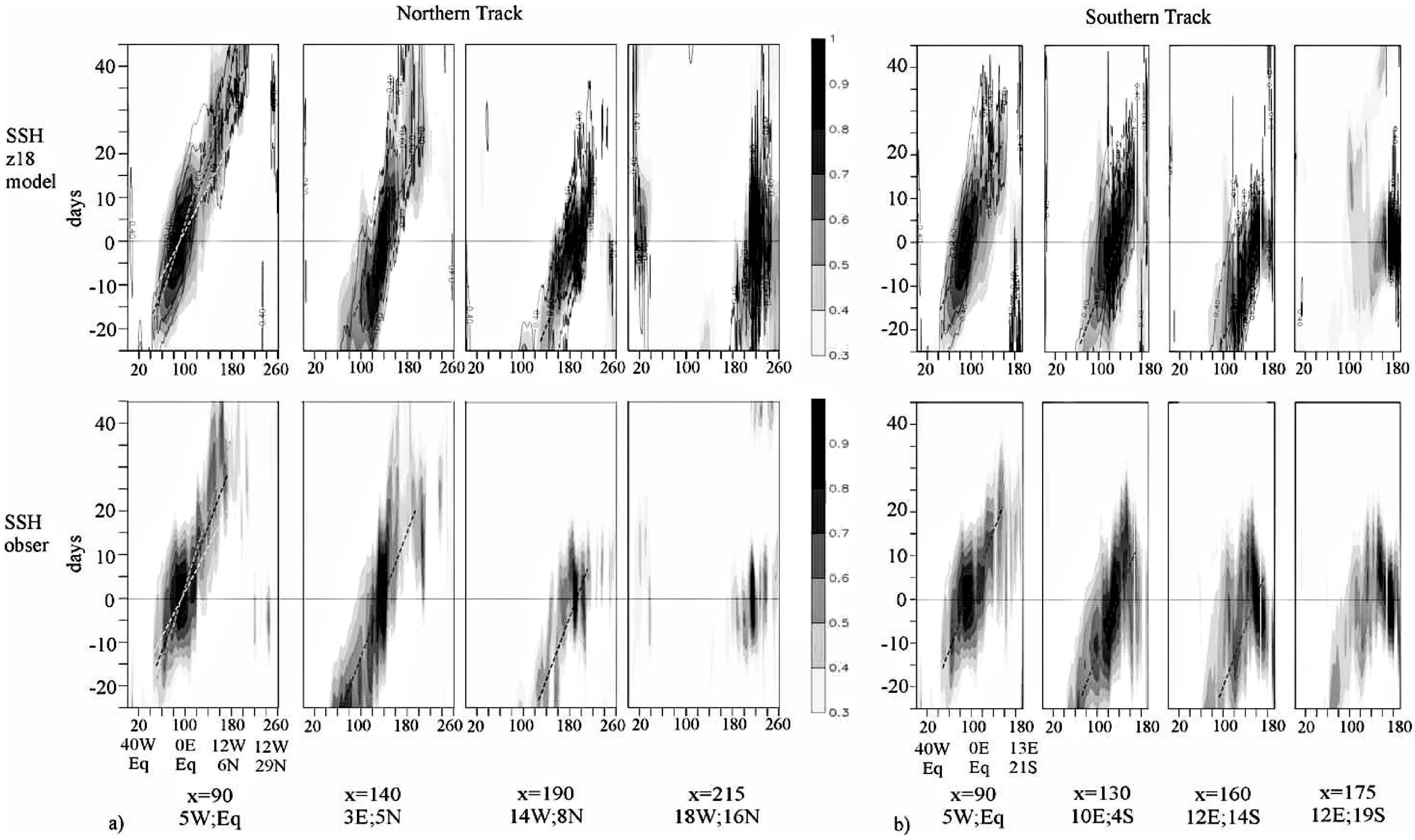
Northern Track
Southern Track
SSH
z18
model
SSH
obser
days
40
20
10
0
-10
-20
20
100
180
260
1
0.9
0.8
0.7
0.6
0.5
0.4
0.3
0.40
40W
Eq
0E
Eq
12W
6N
12W
29N
13E
21S
x=90
5W;Eq
x=140
3E;5N
x=190
14W;8N
x=215
18W;16N
x=90
5W;Eq
x=130
10E;4S
x=160
12E;14S
x=175
12E;19S
a)
b)